Asociación Argentina
de Mecánica Computacional

Mecánica Computacional Vol XXXII, págs. 3677-3689 (artículo completo)
Carlos G. García Garino, Aníbal E. Mirasso, Mario A. Storti, Miguel E. Tornello (Eds.)
Mendoza, Argentina, 19-22 Noviembre 2013

ON ENERGY BUDGET AND TURBULENCE INVESTIGATIONS IN PARTICLE-DRIVEN GRAVITY CURRENTS WITH HIGH-RESOLUTION SIMULATIONS

Luis F. R. Espath[a], Leandro C. Pinto[a], Sylvain Laizet[b] and Jorge H. Silvestrini[a]

[a]*Faculdade de Engenharia, Pontifícia Universidade Católica do Rio Grande do Sul, Av. Ipiranga 6681, 90619-900 Porto Alegre - RS, Brasil - espath@gmail.com*

[b]*Turbulence, Mixing and Flow Control Group, Department of Aeronautics, Imperial College London, London, SW7 2BY, United Kingdom*

Keywords: Energy budget, High-Resolution Simulations, Particle-Driven Gravity Currents.

Abstract. For this work, we are interested in the prediction of a mono-disperse dilute suspension particle-laden flow in the typical lock-exchange configuration using Direct Numerical Simulation (DNS). The main objective of this theoretical and numerical study is to undertake unprecedented simulations in order to focus on the energy budget of the flow and the turbulence characteristics for a range Reynolds number from 2236 up to 10000. For the lower Re case we also consider the density-driven current, that is, without deposition. The energy budget based on governing equations is developed enabling to investigate the full balance between kinetic and potential energy with dissipation terms (due to advective fluid motion and Stokes flow around particles). Also the main features of the flow are presented such as: the temporal evolution of the front location, the sedimentation rate, the resulting streamwise deposit profiles and the shear velocity at the bottom of the channel. The use of Direct Numerical Simulation allows us to investigate the evolution of turbulent structures at the wall, identifying the lobe-and-cleft patterns on the lead of the currents.

1 INTRODUCTION

The phenomenon called gravity currents reveals itself in several ways in nature, either in atmosphere due to sea-breeze fronts, in mountain avalanches of airborne snow or debris flow, or in the ocean due to turbidity currents or river plumes (Simpson (1982)). This kind of flow can be classified as hyperpycnal or hypopycnal flow, accordingly with buoyancy effects present in the currents.

In this numerical study, we focus on particle-driven gravity currents with negative-buoyancy (hyperpycnal flow), where the dynamics play a central role in the formation of hydrocarbon reservoirs (Meiburg and Kneller (2009)). In order to understand the main differences due to deposition an additional density-driven gravity currents simulation, that is, without particles, is carried out. Furthermore, the understanding of the turbulent structures dynamics provides an idea of how the deposition influences the streamwise evolution of the current.

It is clear that the understanding of the physical mechanism associated with these currents as well as the correct prediction of their main features are of great importance for practical and theoretical purposes. For this work, we are interested in the prediction of a mono-disperse dilute suspension particle-driven flow in the typical lock-exchange configuration. We consider only flat surfaces using DNS (Direct Numerical Simulation) for $Re = 2236, 5000, 10000$. Our approach takes into account the possibility of particles deposition but ignores erosion and/or re-suspension. Note that in dilute suspensions, the particle volume fraction is considered relatively small, typically well below 1%.

Previous results were obtained by de Rooij and Dalziel (2001); Gladstone et al. (1998) for this kind of flows were obtained in laboratory experiments, using simplified theoretical models Rottman and Simpson (1983); Bonnecaze et al. (1993), or by numerical simulations (Necker et al. (2002, 2005); Nash-Azadani et al. (2011). It was shown that boundary conditions, initial conditions associated with the lock configuration, and particle sizes can have a strong influence on the main characteristics of this kind of flows. For the case without deposition a large quantity of research have been done in order to understand the basics mechanisms of these currents, particularly the relationship between the front velocity with the Reynolds number for different composition of lock-exchange configurations (Cantero et al. (2007); Ooi et al. (1998)).

The major aim concerning the energy budget of the flow is the evaluation of each term without simplification assumptions, i.e., the energies involved (potential and kinetic) as well as the dissipations (related to potential and kinetic energy variation). Finally we investigate the turbulence structures in such flows for various Reynolds numbers concerning density-driven and particle-driven. Particularly, we will focus on changes occurring in the front of the current. Also, the main features of the flow are related with the temporal evolution of the front location as well as the suspended sediment mass, sedimentation rate and the resulting streamwise deposit profiles.

2 FLOW CONFIGURATION AND GOVERNING EQUATIONS

The lock-exchange flow configuration is used (Figure 1) where uniformly suspended particle sediments are enclosed in a small portion of the dimension domain $L_{1b} \times L_{2b} \times L_{3b}$ separated by a gate with clear fluid. When the gate is removed the particle-fluid mixture flows due to gravity and it undergoes a mutual inverse interaction between the “heavy” particle-mixture flow and the “light” clear fluid. The motion is understood as the transformation from potential energy to kinetic energy.

We assume a dilute suspension of single diameter particles and we do not take into account

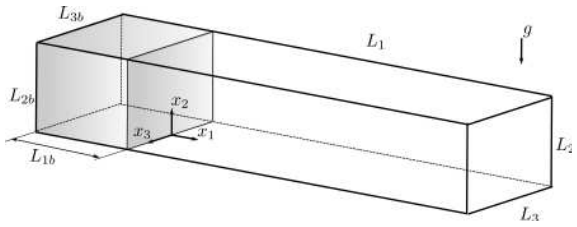

Figure 1: Schematic view of the initial configuration of the lock-exchange flow problem.

the influence of particle inertia and/or particle-particle interaction. It is worth to note that the concentration affect the mixture viscosity, however this effect is neglected. Nevertheless, all these premises are completely valid within the framework of the dilute suspension.

With the restriction imposed by the dilute suspension approach, this flow can be evaluated numerically by solving the Navier-Stokes and scalar transport equations under the Boussinesq approximation. Also, these assumptions allow to relate the particle diameter with the settling velocity. To make these equations dimensionless, half of the box height is chosen (Figure 1) as the characteristic length scale h and the buoyancy velocity u_b is chosen as the velocity scale. The buoyancy velocity is related to the reduced gravitational acceleration $u_b = \sqrt{g'h}$ where $g' = g(\rho_p - \rho_0)c_i/\rho_0$. The particle and clear fluid densities are ρ_p, ρ_0 respectively, with g being the gravitational acceleration and c_i the initial volume fraction of the particles in the lock. When introducing the velocity and length scales two dimensionless numbers appear in the equations: the Reynolds number defined as $Re = u_b h/\nu$ where ν is the kinematic viscosity of the fluid, and the Schmidt number $Sc = \nu/k$, where k is the mass diffusivity of the particle-fluid mixture. All other parameters and variables are made dimensionless using c_i, h or/and u_b. Thus, the dimensionless form for the governing equation are

$$\mathbf{div}\,(\underline{\mathbf{u}}) = 0 \tag{1a}$$

$$\frac{\partial \underline{\mathbf{u}}}{\partial t} + \underline{\mathbf{u}} \cdot \nabla \underline{\mathbf{u}} = \frac{2}{Re}\mathbf{div}\,(\underline{\mathbf{s}}) - \nabla p + c\,\underline{\mathbf{e}}^g \tag{1b}$$

$$\frac{\partial c}{\partial t} + (\underline{\mathbf{u}} + u_s\,\underline{\mathbf{e}}^g)\,\nabla c = \frac{1}{ScRe}\nabla^2 c \tag{1c}$$

where $\underline{\mathbf{e}}^g = (0, -1, 0)$ is the unit vector in gravity direction and the nondimensional quantities $\underline{\mathbf{u}}, p, c, \underline{\mathbf{s}}$ represent the fluid velocity, pressure, particle concentration and strain rate tensor fields, respectively. The particle settling velocity u_s is related to the particle diameter by the Stokes settling velocity law.

Initial conditions are defined introducing a weak perturbation on the velocity field in the neighbourhood of the interface in order to mimic the disturbances introduced in the flow when the mixture is released. Free-slip boundary conditions are imposed for the velocity field in the streamwise and spanwise directions. No-slip boundary conditions are used in the vertical direction. For the scalar, no-flux conditions are used in the streamwise and spanwise directions and in the vertical direction at the top of the domain. In order to take into account the particles deposit in the vertical direction at the bottom of the domain, an outflow boundary condition is used, $\frac{\partial c}{\partial t} + u_s e_2^g \frac{\partial c}{x_2} = 0$, which allows particles to leave the computational domain mimicking a deposition process. It should be noticed that no re-suspension is allowed. In density-driven case, any wall has no-flux boundary condition for scalar equation and settling velocity is zero, $u_s = 0$.

3 ENERGY BUDGET OF THE FLOW

The energy budget of the flow for an incompressible flow with particle concentration in the dilute suspension approach is established from Equations (1a,1b,1c). It is interesting to split the total energy in the kinetic and potential energy, in addition, the dissipation associated to the gradients in the macroscopic advective motion and also the dissipation that occurs in the microscopic Stokes flows around the particles.

The resulting time derivative of the kinetic energy equation is derived from the multiplication of the momentum equation (1b) by $\underline{\mathbf{u}}$ yielding

$$\frac{\mathrm{D}\left(\frac{1}{2}\underline{\mathbf{u}}\cdot\underline{\mathbf{u}}\right)}{\mathrm{D}t} = -\mathbf{div}\left(p\underline{\mathbf{u}}\right) + \frac{2}{Re}\mathbf{div}\left(\underline{\underline{\mathbf{s}}}\cdot\underline{\mathbf{u}}\right) - \frac{2}{Re}\underline{\underline{\mathbf{s}}} : \underline{\underline{\mathbf{s}}} - u_2 c \tag{2}$$

where $\frac{\mathrm{D}(\cdot)}{\mathrm{D}t}$ is the material derivative. Integrating Equation (2) over the entire domain Ω, gives

$$\frac{dk}{dt} = -\int_\Omega \frac{2}{Re}\underline{\underline{\mathbf{s}}} : \underline{\underline{\mathbf{s}}}\,\mathrm{d}\Omega - \int_\Omega u_2 c\,\mathrm{d}\Omega \tag{3}$$

where $k\left(t\right) = \int_\Omega \frac{1}{2}u_i u_i\,\mathrm{d}\Omega$. It is important to note that any integral of a divergence field over the domain is null, since there is no transport across the boundaries.

On the other hand, the potential energy is expressed as

$$E_p\left(t\right) = \int_\Omega c x_2\,\mathrm{d}\Omega \tag{4}$$

and its variation with time is derived from the multiplication of the transport equation of the particle concentration (1c) by x_2 yielding

$$\frac{\mathrm{D}c}{\mathrm{D}t}x_2 = \frac{1}{ScRe}x_2\nabla^2 c + x_2 u_s\frac{\partial c}{\partial x_2} \tag{5}$$

Integrating over the entire domain Ω, gives

$$\frac{dE_p}{dt} = \int_\Omega \frac{D\left(cx_2\right)}{Dt}\,\mathrm{d}\Omega = \int_\Omega \left(\frac{1}{ScRe}x_2\nabla^2 c + x_2 u_s\frac{\partial c}{\partial x_2}\right)\mathrm{d}\Omega + \int_\Omega u_2 c\,\mathrm{d}\Omega \tag{6}$$

From Equations (3) and (6), i.e., $\frac{d(k+E_p)}{dt}$, the exact dissipation terms are defined as:

$$\begin{aligned}\frac{d\left(k+E_p\right)}{dt} &= -\int_\Omega \frac{2}{Re}\underline{\underline{\mathbf{s}}} : \underline{\underline{\mathbf{s}}}\,\mathrm{d}\Omega \\ &\quad + \int_\Omega \left(\frac{1}{ScRe}x_2\nabla^2 c + x_2 u_s\frac{\partial c}{\partial x_2}\right)\mathrm{d}\Omega \\ &= -\epsilon - \epsilon_s\end{aligned} \tag{7}$$

where ϵ is related to the turbulent dissipation (macro-dissipation) while ϵ_s is the dissipation associated with loss of energy due to suspended particles (micro-dissipation). These instantaneous dissipations terms can be integrated in time in order to evaluate the total dissipation,

$$\begin{aligned}E_d &= -\int_0^\tau \epsilon\,d\tau \\ E_s &= -\int_0^\tau \epsilon_s\,d\tau\end{aligned} \tag{8}$$

Table 1: Summary of numerical parameters.

Re	L_1, L_2, L_3	n_1, n_2, n_3	Δt	deposition
2236	$18, 2, 2$	$1441, 221, 201$	6.024×10^{-4}	no
2236	$18, 2, 2$	$1441, 221, 201$	6.024×10^{-4}	yes
5000	$18, 2, 2$	$1537, 257, 257$	5×10^{-4}	yes
10000	$18, 2, 2$	$2305, 513, 385$	3×10^{-4}	yes

Now one can evaluate the total energy of the currents with

$$E_T = E_p + k + E_d + E_s = E_{T_0} = E_{p_0} + k_0 + E_{d_0} + E_{s_0} = \text{constant} \tag{9}$$

A similar derivation with simplifying assumptions may be found in Necker et al. (2005), the main difference is that we compute the exact energy equation (7) without any assumption over the dissipation terms.

4 NUMERICAL METHOD AND PARAMETERS

The in-house code `Incompact3d` is used, in order to solve numerically the governing equations (1a,1b,1c) developed by Laizet and Lamballais (2009). It is based on compact sixth-order finite difference schemes for spatial differentiation and a third-order Adams-Bashforth scheme for time integration. To treat the incompressibility condition, a fractional step method requires to solve a Poisson equation. This equation is fully solved in spectral space via the use of relevant 3D Fast Fourier Transforms. More information about the code can be found in Laizet and Lamballais (2009). For the three-dimensional simulations presented here, the parallel version of `Incompact3d`, based on a powerful 2D domain decomposition is used. More details about this domain decomposition can be found in Laizet and Li (2011).

The main numerical parameters for the simulations are shown in Table 1, In all cases we use an uniform grid where the numbers of mesh nodes and the size of the simulations have been carefully chosen in order to solve the smallest scales of the flow. We consider $(L_{1b}, L_{2b}, L_{3b}) = (1h, 2h, 2h)$ to define the box containing the particle-fluid mixture. The settling velocity is set to $u_s = 0.02$ in order to correspond with a middle silt, $43.5\mu m$, while the Schmidt number is fixed in $Sc = 1$. All the simulations were run for $t = 60$ except the $Re = 10000$ which was stopped at $t = 32$ in order to limit the computational effort. The perturbation added to the initial velocity field is adjusted to yield an initial kinetic energy about 1% of the initial potential energy.

It should be noted that the $Re = 2236$ case is similar to the numerical work of Necker et al. (2002). The only difference lies in the way the weak perturbation is added as initial condition to the velocity field. The $Re = 10000$ case is very close to the experimental configuration of de Rooij and Dalziel (2001).

5 RESULTS

In this section, a selection of results are presented, concerning analysis of turbulence structures of the flow, global quantities related to front location, suspended material, sedimentation rate, streamwise particle deposits and the energy budget of the flow. We also focus on the description of the local and instantaneous main features of the particle-driven gravity current

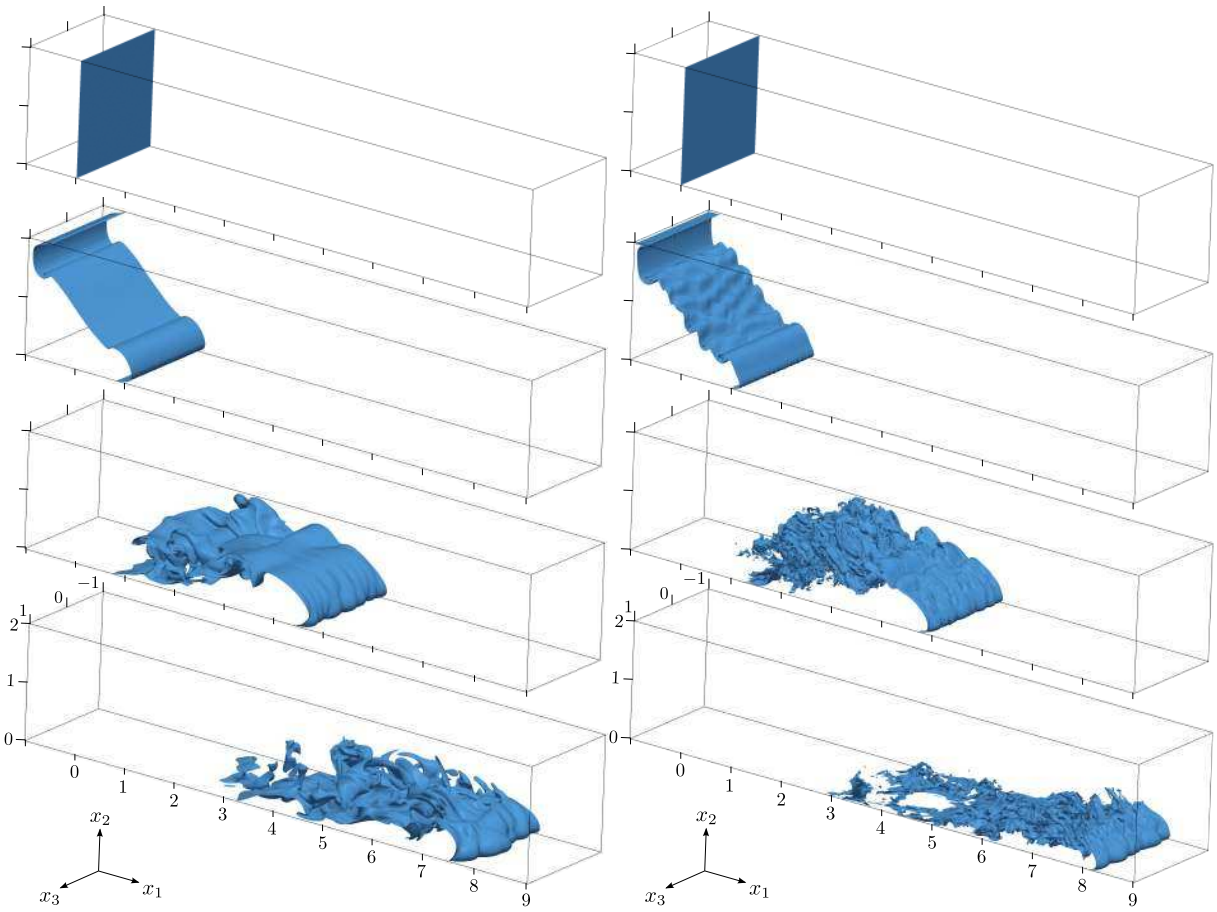

Figure 2: Interface evolution between particle-fluid and clear fluid for $t = 0, 2, 8, 14$ (from top to bottom) for a concentration $c = 0.25$ (left $Re = 2236$; right $Re = 10000$).

front, characterized by the so-called lobe-and-cleft instability (Härtel et al. (2000)) and on the spatial distribution of the shear stress over the bottom channel for different Re numbers and considering the cases with and without particle settling.

5.1 Turbulent structures in gravity currents

The sudden release of the particle-fluid mixture along the left wall (figure 2) leads to the streamwise evolution of the gravity current into the clear fluid. There are two mechanisms yielding the motion: the first one is occasioned by transformation of the potential energy in kinetic energy, leading to a advective motion, and the second one is the diffusivity motion proportioning the mixture that occurs by the potential difference between heavy- and clear-fluid.

Due to the small amount of kinetic energy at $t = 0$, this motion is initially two-dimensional for the low Re case ($Re = 2236$) while clearly three-dimensional perturbations are already present for the high Re number case ($Re = 10000$). This fact can be verified comparing the pictures for $t = 2$ in Figure 2. After that, three-dimensional structures can be observed at the head and at the tail of the current.

At $t = 8$ the turbulent structure of the front and of the tail are well defined by lobe-and-cleft and Kelvin-Helmholtz instabilities, as shown at the left side of Figure 3. While, at $t = 14$ the gravity current develops a highly 3D turbulence with intense streamwise vortices as shown

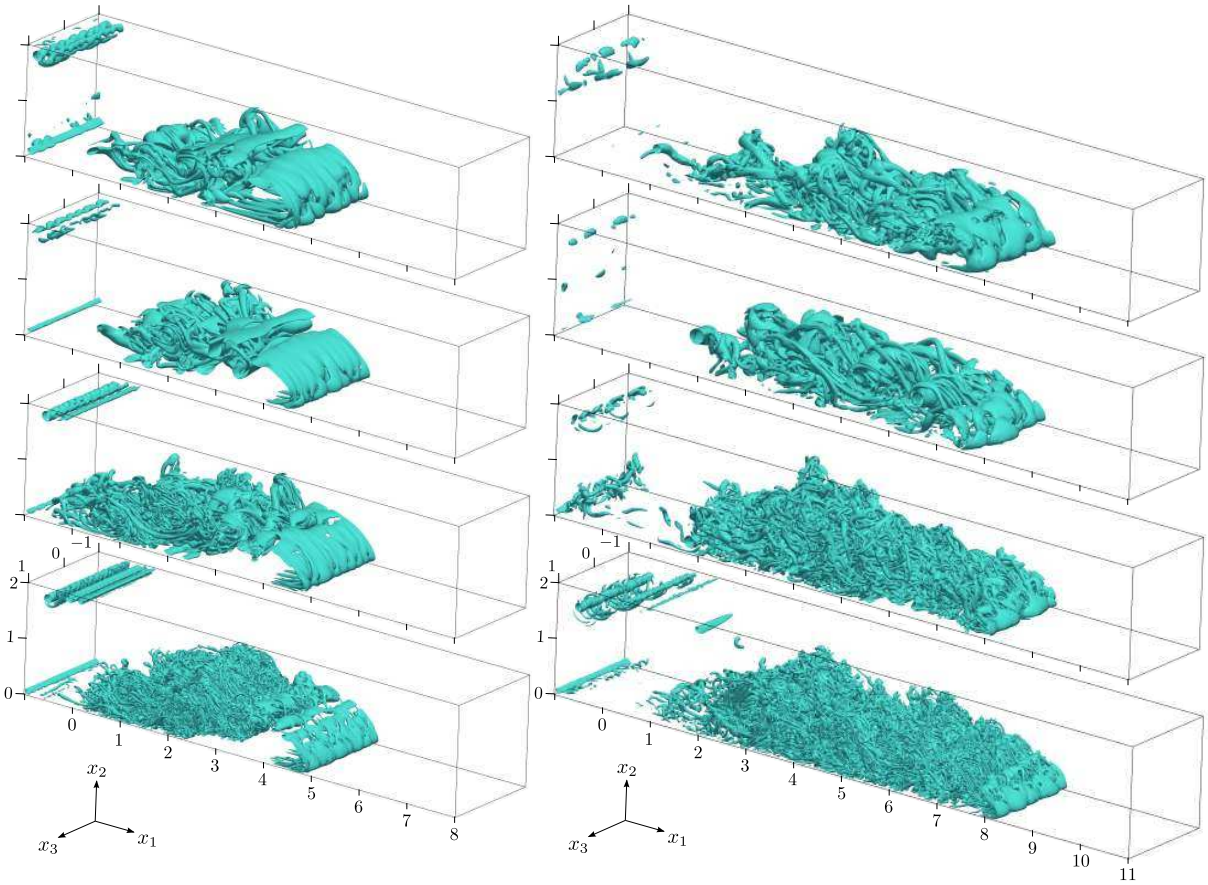

Figure 3: Turbulent structure of the gravity currents by isosurfaces of $Q-$criterion (for the isovalue $Q = 1$) from top to bottom: $Re = 2236$ (density-driven) and $Re = 2236, 5000, 10000$ (particle-driven) at $t = 8$ (left) and $t = 14$ (right).

in the $Q-$criterion pictures at the right side of Figure 3. Therefore, it can be seen a higher level of turbulence with smaller and very intense structures for the $Re = 10000$ simulation by comparison with the lower Re simulations.

In Figure 4 snapshots of the concentration field are shown for $t = 14$ and $t = 20$ for the $x_3 = 0$ middle-plane for the four simulations considered. It can be seen some important characteristic; concerning simulations with deposition one can observe that concentration is located near the bottom wall, in addition mixing capability is appreciated when the Reynolds number increases. On the other hand, the density-driven case, that is, without deposition, shows a large spreading of the current with a high front velocity at $t = 20$.

5.2 Global results for simulations with deposition

A set of global quantities is computed in order to understand the main features of this transient flow. The temporal evolution for the front location, suspended particles mass, sedimentation rate, deposit profiles at the bottom of the box and energy budget of the flow are compared with the numerical predictions obtained by Necker et al. (2002) and with the experimental data of de Rooij and Dalziel (2001).

At the left side of Figure 5 the time evolution of the front location, x_f, and the suspended mass normalized by the initial suspended mass, m_p/m_{p_0} are shown. In this figure is also presented the sedimentation rate (at the right side). Concerning the front position, it can be ob-

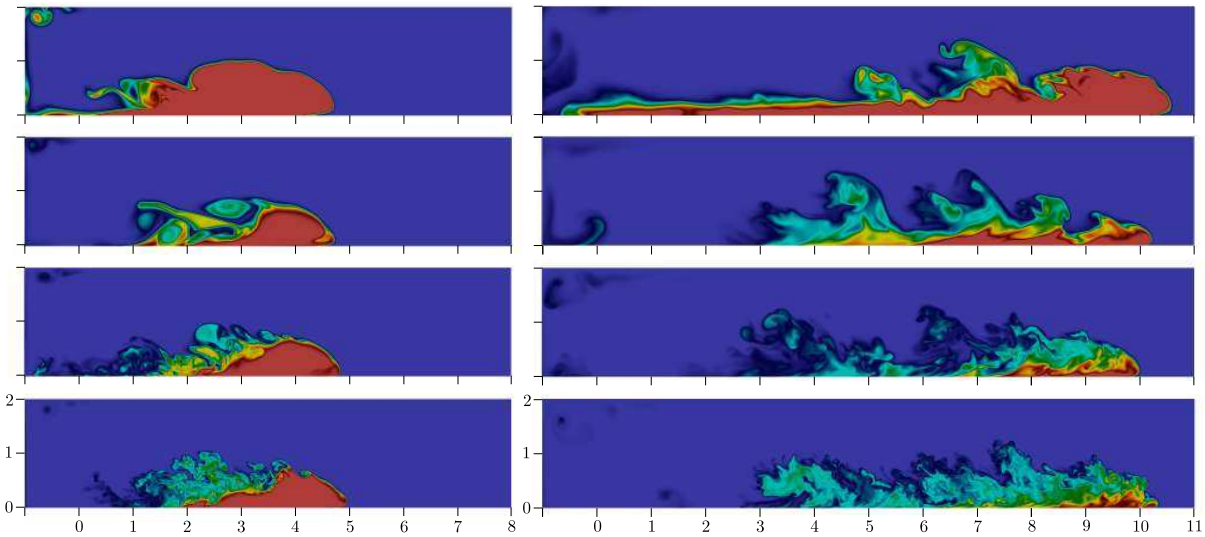

Figure 4: Particle concentration fields at $t = 14$ (left) and $t = 20$ (right) for $Re = 2236$ without deposition and $Re = 2236, 5000, 10000$ with deposition (from top to bottom) in the $x_3 = 0$ middle plane. Snapshots taken for $0 < c < 0.3$.

served that the particle-driven gravity current has a constant front velocity until time $t \approx 10$, similar to density-driven current without particles. After $t \approx 10$ the front velocity deviates from the straight line due to particles settling.

The sedimentation rate can be evaluated as

$$\dot{m}_s = \frac{1}{L_1 L_3} \int_0^{L_1} \int_0^{L_3} c_w(x_1, x_3, t) u_s dx_3 dx_1, \tag{10}$$

where c_w accounts for the sediment concentration at the bottom channel.

Regarding the sedimentation rate (right side of Figure 5), two power laws can be identified, separated by a peak value around $t \approx 15$. This behaviour occurs independently of Reynolds number, however there is a delay in the peak occurrence when Reynolds number is decreased. The peak occurs when $\approx 50\%$ of the suspended particles are already settled.

Another global quantity of extremely importance for practical implications is the streamwise deposit of sediment particles computed as

$$D_t(x_1, t) = \int_0^t < c_w(x_1, \tau) >_{x_3} u_s \, d\tau, \tag{11}$$

where $< \ . \ >_{x_3}$ indicated a mean value in the x_3 direction. Figure 6 shows this quantity in function of the streamwise coordinate x_1. The deposit is normalized with the deposit for the final time $t = 60$. The selected times are $t = 7.3, 10.95, 60$, in order to compare with available experimental data. Note that the DNS for $Re = 10000$ was stopped at $t = 32$ to limit the computational effort. With this choice, the present results cannot be compared both with the numerical data of Necker et al. (2002) and the experimental data of de Rooij and Dalziel (2001), once the deposit is normalized with the total deposit at $t = 60$, i.e., the area of the final deposit is set to one. A global good agreement between experimental data and numerical results can be seen in this figure. The results for $Re = 5000$ are very close to the experimental data both at initial and final times of the simulation. The differences at the left channel side can be attributed to different initial conditions between laboratory experiments and numerical simulations.

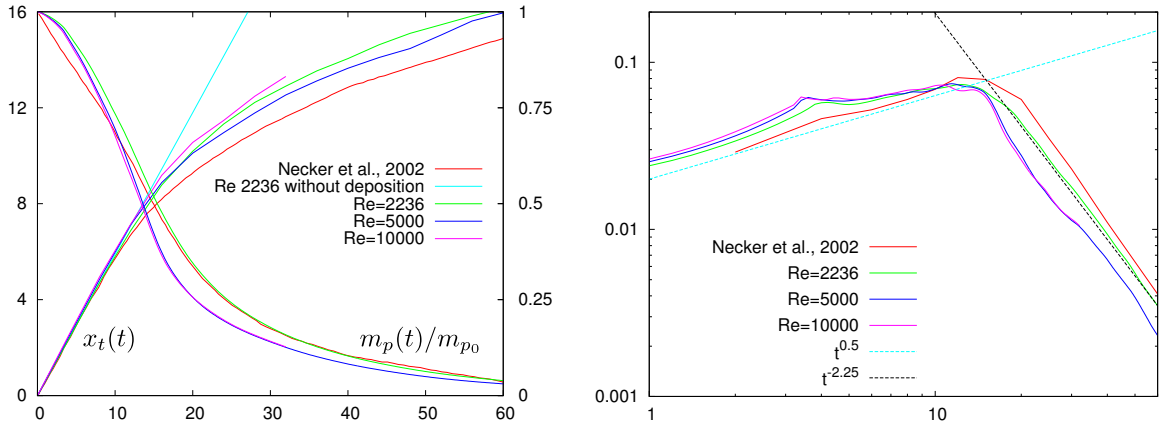

Figure 5: Front location x_f and suspended particles m_p/m_{p_0} as a function of time (left) Sedimentation rate $\dot{m}_s(t)$ as function of time (right) with comparisons with the numerical data of Necker et al. (2002)..

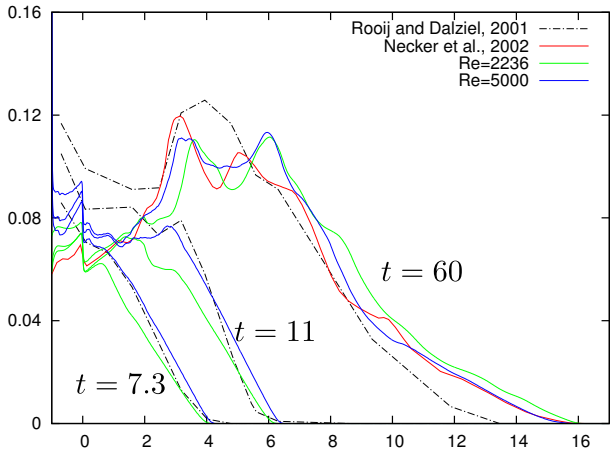

Figure 6: Deposit profiles for $t = 7.3, 11, 60$ for $Re = 2236, 5000$ with comparisons with the numerical data of Necker et al. (2002) and experimentals data of de Rooij and Dalziel (2001).

In Figure 7 is shown the energy budget, concerning the time evolution of potential E_p, kinetic energies k, micro- E_s and macro-dissipations E_d compared with the predictions obtained by Necker et al. (2002). All quantities are normalized by the total initial energy. Concerning the three different Reynolds number, the main differences are observed in the maximum level o kinetic energy and the dissipation due to the advective motion.

5.3 Wall turbulence characteristics

At the bottom wall of the channel, increasing spanwise motions cause lobe-and-cleft structures at the current front location. This complex structure was observed in many experiments (Simpson (1982)) and more recently in the DNS of density-driven current (without suspended particles) of Härtel et al. (2000) and Cantero et al. (2007) and the particle-driven simulations of Necker et al. (2002).

In Figure 8, the wall shear velocity field at the wall is shown for $t = 8$, computed as $\left|s\right|_w = \sqrt{\left(\partial u_1/\partial x_2\right)^2 + \left(\partial u_3/\partial x_2\right)^2}|_{x_2=0}$. It is formed by zones of high shear velocity, the lobe region,

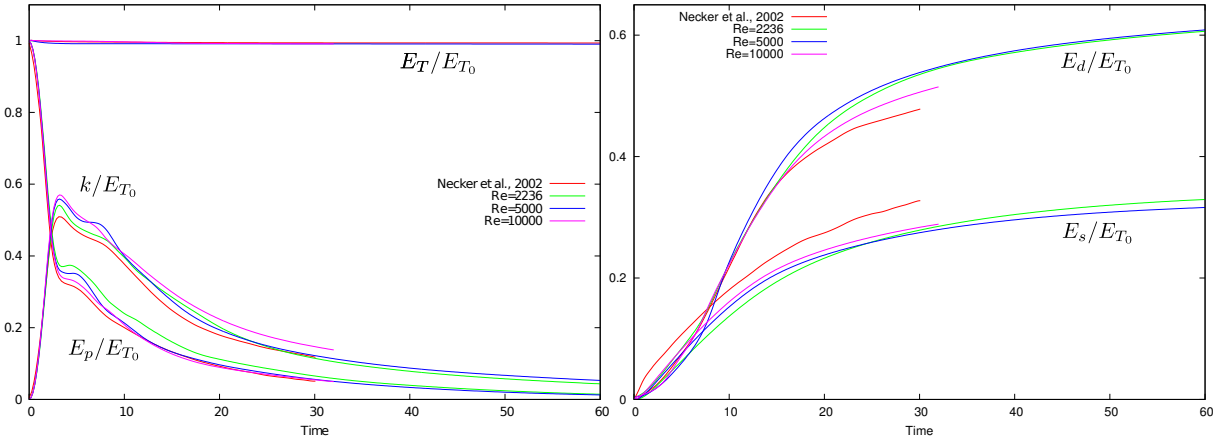

Figure 7: Time history of the kinetic k and potential E_p energy (left) and macro- and micro-dissipation (right) for the three Re numbers with comparisons with the numerical data of Necker et al. (2002).

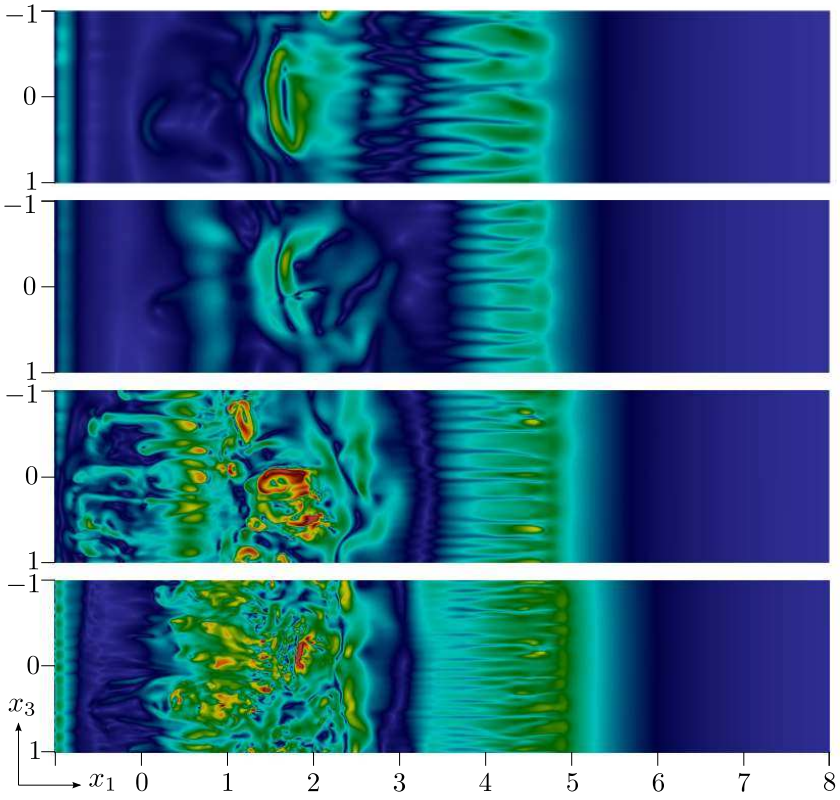

Figure 8: Wall shear velocity at $t = 8$ for $Re = 2236$ without deposition and for $Re = 2236, 5000, 10000$ with deposition (from top to bottom). $0 < |s|_w < 15$.

alternating with regions of low values, the cleft region. This spatial organization of the wall shear velocity can be correlated with other physical phenomena, not considered in the present simulations. Regions of intense vertical gradient are good candidates to undergo local erosion processes.

More intense activity at the front but also for $0.5 < x_1 < 2.5$ (the body and the tail of the currents) can be observed when the Re number is increased. Regarding the characteris-

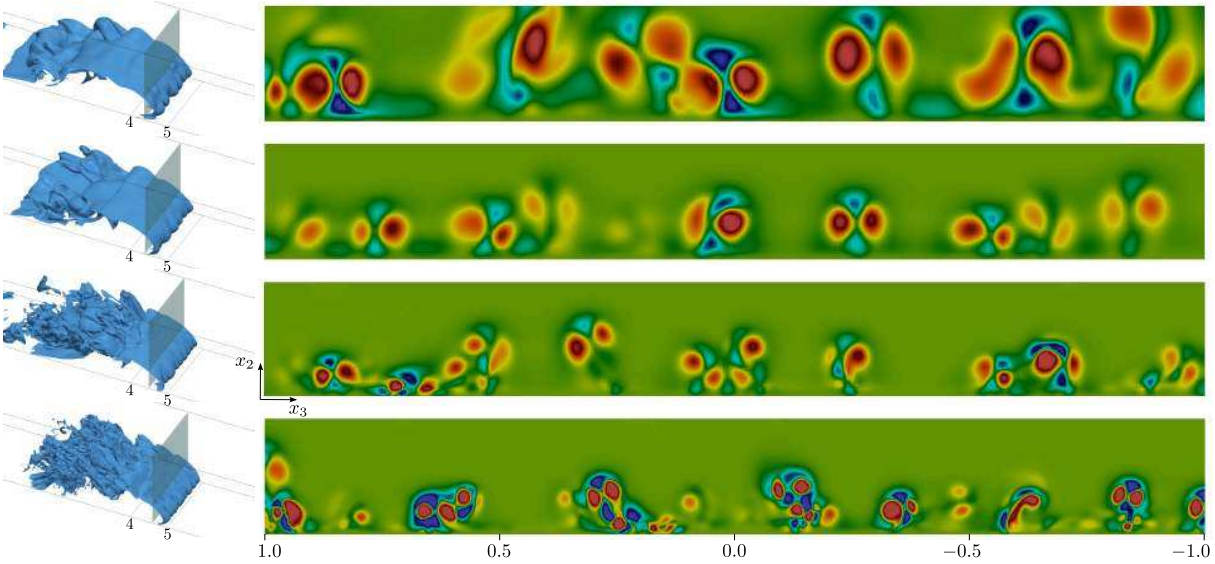

Figure 9: Structure of the front by isosurface for $c = 0.25$ (left) and Q-criterion with isovalues ranging from $-25 < Q < 25$ (right) at $t = 8$. The plane is located at a distance of $0.33h$ behind the front of the current. From top to bottom: $Re = 2236$ (density-driven), $Re = 2236,\ 5000$ and 10000 (particle-driven). Red indicates $Q > 0$ and blue $Q < 0$.

tic dimension of the lobe in the spanwise direction, it is important to note that: when the Re increases, the lobe dimension decreases. Furthermore, the cleft dimension in spanmwise direction has the same behaviour, analysing particle-driven cases. On other hand, the cleft dimension in streamwise direction increases when Re increases. Comparing the particle-driven with the density-driven for the same Re is worth to notice that the strain rate level measured at the wall is slightly lower for the particle-driven case, furthermore, the cleft shows shorter when compared with the density-driven case.

At $t = 8$ the structure of the particle-laden gravity current front can be analysed through the visualization of the concentration field as it is shown on the left side picture of Figure 9. The isovalue chosen is $c = 0.25$. At the right side of the same picture, a cross section of $Q-$criterion for the selected vertical planes just behind the current front is shown. From this figure, the lobe-and-cleft instability can be already identified in the region limited by pairs of streamwise vortices associated with positive values of $Q-$ criterion (indicated in red). The picture also shows how these streamwise vortices become thinner and more intense when the Re number is increased. Also in the picture, the blue zone, where $Q < 0$, denotes a region where the strain rate overcomes the rotation rate.

On one hand, Figure 9 suggests that clefts are related to high strain rate region whereas lobes are limited by zones of intense rotation rate. But on the other hand, the strain rate measured at the bottom wall (see for instance Figure 8) is higher in the lobe zone, while in the cleft zone there is no an important strain rate. This information about the lobe-and-cleft was condensed in Figure 10. One can compare the turbulent structures for $Re = 2236$ with and without deposition and conclude that the structures that define a lobe are bigger and taller for density-driven case.

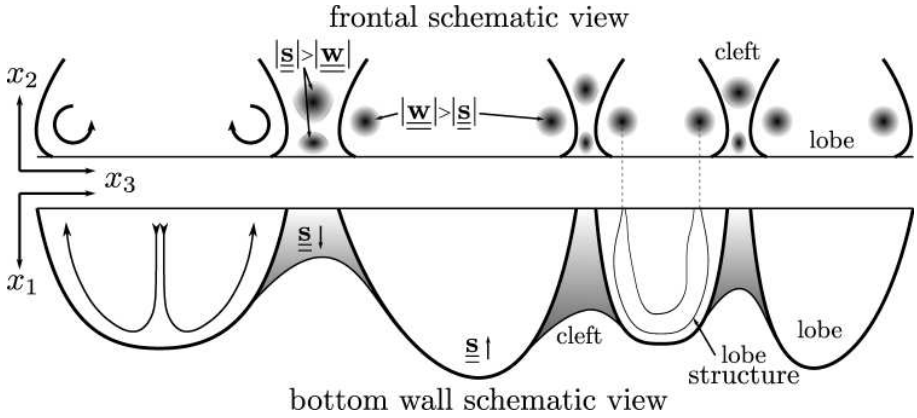

Figure 10: Schematic representation of lobe-and-cleft pattern.

6 CONCLUSIONS

The main features of a particle-driven gravity current for a dilute suspension in a lock-exchange configuration were examined using 3D DNS. In addition, one simulation of a density-driven gravity current was analysed in order to understand the head and the body of the currents when compared with particle-driven case. Three Re numbers were considered allowing direct comparisons with published experimental and numerical data. The main results are related with the streamwise length and suspended sediment mass of the current front, the time evolution of sedimentation rate and the resulting particle deposit at the channel wall. Good global agreements were found with published results. In addition, we analysed the lobe-and-cleft patterns on the lead of the currents, from the evolution of turbulent structures at the wall.

7 ACKNOWLEDGEMENTS

Present simulations have been carried out at the LAD/PUCRS in Porto Alegre. The authors are grateful to Petrobras for supporting this research. JS acknowledges financial assistance of CNPq.

REFERENCES

Bonnecaze R., Huppert H., and Lister J. Particle-driven gravity currents. *J. Fluid Mech.*, **250**:339–369, 1993.

Cantero M., Balachandar S., and Garcia M. High-resolution simulations of cylindrical density currents. *J. Fluid Mech.*, **590**:437–469, 2007.

de Rooij F. and Dalziel S. Time- and space-resolved measurements of deposition under turbidity currents. *Spec. Publs. Int. Ass. Sediment.*, **31**:207–215, 2001.

Gladstone C., Phillips J., and Sparks R. Experiments on bidisperse, constant-volume gravity currents: propagation and sediment deposition. *Sedimentology*, **45**:833–843, 1998.

Härtel C., Carlsson F., and Thunblom M. Analysis and direct numerical simulation of the flow at a gravity-current head. Part 2. The lobe-and-cleft instability. *J. Fluid Mech.*, **418**:213–229, 2000.

Laizet S. and Lamballais E. High-order compact schemes for incompressible flows: A simple and efficient method with the quasi-spectral accuracy. *J. Comp. Phys.*, **228**:5989–6015, 2009.

Laizet S. and Li N. Incompact3d: A powerfull tool to tackle turbulence problems with up to O(10^5) computational cores. *Int. J. Heat and Fluid Flow*, **67**:1735–1757, 2011.

Meiburg E. and Kneller B. Turbidity currents and their deposits. *Annu. Rev. Fluid Mech.*, **42**:135–156, 2009.

Nash-Azadani M., Hall B., and Meiburg E. Polydisperse turbidity currents propagating over complex topography: Comparison of experimental and depth-resolved simulation results. *Computers and Geosciences*, :doi:10.1016/j.cageo.2011.08.030, 2011.

Necker F., Hartel C., Kleiser L., and Meiburg E. High-resolution simulations of particle-driven gravity currents. *Int. J. Multiphase Flow*, **28**:279–300, 2002.

Necker F., Härtel C., Kleiser L., and Meiburg E. Mixing and dissipation in particle-driven gravity currents. *J. Fluid Mech.*, **545**:339–372, 2005.

Ooi S.K., Constantinescu G., and Weber L. Numerical simulations of lock-exchange compositional gravity current. *J. Fluid Mech.*, **635**:361–388, 1998.

Rottman J. and Simpson J. Gravity currents produced by instantaneous releases of a heavy fluid in a rectangular channel. *J. Fluid Mech.*, **135**:95–110, 1983.

Simpson J.E. Gravity currents in the laboratory, atmosphere and ocean. *Annu. Rev. Fluid Mech.*, **14**:213–234, 1982.